# LETTER

# The emergence of functional microcircuits in visual cortex

Ho Ko[1]*, Lee Cossell[1]*, Chiara Baragli[1], Jan Antolik[1]†, Claudia Clopath[2], Sonja B. Hofer[1]* & Thomas D. Mrsic-Flogel[1]*

Sensory processing occurs in neocortical microcircuits in which synaptic connectivity is highly structured[1–4] and excitatory neurons form subnetworks that process related sensory information[5,6]. However, the developmental mechanisms underlying the formation of functionally organized connectivity in cortical microcircuits remain unknown. Here we directly relate patterns of excitatory synaptic connectivity to visual response properties of neighbouring layer 2/3 pyramidal neurons in mouse visual cortex at different postnatal ages, using two-photon calcium imaging *in vivo* and multiple whole-cell recordings *in vitro*. Although neural responses were already highly selective for visual stimuli at eye opening, neurons responding to similar visual features were not yet preferentially connected, indicating that the emergence of feature selectivity does not depend on the precise arrangement of local synaptic connections. After eye opening, local connectivity reorganized extensively: more connections formed selectively between neurons with similar visual responses and connections were eliminated between visually unresponsive neurons, but the overall connectivity rate did not change. We propose a sequential model of cortical microcircuit development based on activity-dependent mechanisms of plasticity whereby neurons first acquire feature preference by selecting feedforward inputs before the onset of sensory experience—a process that may be facilitated by early electrical coupling between neuronal subsets[7–9]—and then patterned input drives the formation of functional subnetworks through a redistribution of recurrent synaptic connections.

Intrinsic and experiential factors guide the patterning of neural pathways and the establishment of sensory response properties during postnatal development[10–12]. During this time, neural circuit refinement is thought to depend on the elimination of initially exuberant projections, selective formation of new connections or both[13,14]. However, the mechanisms governing the emergence of structured connectivity in local cortical microcircuits, where dendrites and axons overlap extensively, remain uncertain. Moreover, it is not clear whether the organization of synaptic connections between nearby neurons is established early and inherently linked to the formation of receptive fields (RFs) before the onset of sensory experience or whether the mature patterns of recurrent connectivity appear only after the formation of RFs as a result of correlated activity induced by feedforward drive from the sensory periphery. Here we investigate these questions in networks of layer 2/3 (L2/3) pyramidal cells in mouse primary visual cortex (V1)—where neighbouring neurons exhibit a diversity of preference for visual features[5,15–17]—by determining how local synaptic connectivity relates to visual response properties during development.

Stimulus-selective responses in V1 are observed at eye opening[18–22], but the extent to which detailed RFs are established by this time remains unclear. To characterize the spatial RF structure of L2/3 neurons in V1 at eye opening (postnatal days (P) 14–15) and in more mature mice (P28–35), we used *in vivo* two-photon calcium imaging[23]

in monocular V1 to obtain spatial RFs by reverse correlation[16,17,24] of static natural images and spiking responses inferred from calcium signals[25] (Methods and Fig. 1a, b), and fitted a two-dimensional Gabor function to the RFs (Supplementary Fig. 1). At eye opening, L2/3 neurons exhibited a diversity of RF spatial structures that resembled those of mature V1 neurons (Fig. 1c and Supplementary Fig. 1a). The proportion of neurons with significant linear RFs was similar between the two age groups (P14–15, 60%, 191 of 317; P28–35, 58%, 201 of 348; $P = 0.51$, $\chi^2$ test; Fig. 1d), as was the angle of visual space subtended by RFs (mean visual angle along the long RF axis ± s.d.: P14–15, $29.3 \pm 13.6°$; P28–35, $29.4 \pm 10.3°$; $P = 0.12$, rank-sum test; Fig. 1e; see also Supplementary Fig. 1b, c). The similarity of RF structures was shown by the overlapping distributions of standard RF measures of $n_x$ and $n_y$, which respectively express the width and length of the fitted Gabor function in units of the underlying grating period (median $n_x$: P14–15, 0.31; P28–35, 0.32; $P = 0.14$; median $n_y$: P14–15, 0.20; P28–35, 0.20; $P = 0.41$; rank-sum test; Methods and Supplementary Fig. 1d). For comparison, the orientation tuning of neurons responsive to drifting gratings was slightly but significantly broader at eye opening than in more mature V1 (median orientation selectivity index: P13–15, 0.62; P22–26, 0.68; $P = 2.39 \times 10^{-34}$, rank-sum test; Supplementary Fig. 2a, b). Neuronal responses at eye opening, however, exhibited higher variability to repeated presentation of the preferred grating stimulus (coefficient of variation (CV)) than in more mature animals (mean CV ± s.d.: P13–15, $0.93 \pm 0.36$; P22–26, $0.71 \pm 0.30$; $P = 1.17 \times 10^{-304}$, rank-sum test; Supplementary Fig. 2c), indicating that responses in immature animals were less reliable despite the presence of clearly defined RFs and orientation selectivity.

The similarity of spatial RF properties in immature and older V1 suggests that the organization of feedforward connections[26] was largely established by the time of eye opening. We next tested whether the synaptic connectivity of neurons in the local cortical network is functionally specific when vision begins. We combined *in vivo* two-photon calcium imaging in V1 and subsequent multiple whole-cell recordings in slices of the same tissue[5] (Fig. 2). We first imaged calcium signals at consecutive depths within L2/3 to characterize the responses to natural movies and drifting gratings (Methods) of all neurons within a volume of approximately $285 \mu m \times 285 \mu m \times 40–120 \mu m$. We then carried out simultaneous whole-cell recordings *in vitro* from two to six neighbouring L2/3 pyramidal neurons separated by less than $50 \mu m$ (mean distance ± s.d.: P13–15, $24 \pm 9 \mu m$; P22–26, $25 \pm 10 \mu m$; Fig. 2a, b). We recorded from 143 and 140 neurons in total in the slices at P13–15 and P22–26, respectively, which were identified in the *in vivo* image stack by image registration based on affine transformation[5] (Fig. 2a). Synaptic connectivity was assessed by evoking action potentials in each neuron sequentially while searching for the presence of excitatory postsynaptic potentials in the other neurons (Fig. 2b). This approach allowed us to relate the probability of finding connections between pairs of L2/3 neurons to the correlation of their average responses to

[1]Department of Neuroscience, Physiology and Pharmacology, University College London, 21 University Street, London WC1E 6DE, UK. [2]Center for Theoretical Neuroscience, Columbia University, 1051 Riverside Drive, Unit 87 Kolb Research Annex, New York, New York 10032, USA. †Present address: Unité de Neuroscience Information et Complexité, UPR 3293 CNRS, 1 Avenue de la Terrasse, 91198 Gif-sur-Yvette, France.
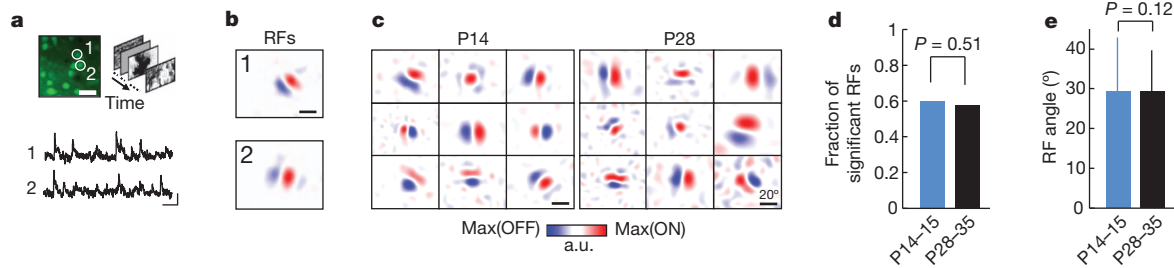*These authors contributed equally to this work.

**Figure 1 | Responses of L2/3 pyramidal cells in mouse visual cortex are highly feature selective at eye opening. a**, Example of OGB-labelled region at P14 (left; scale bar, 30 μm) with calcium transients of two cells obtained with two-photon microscopy (bottom; scale bars, 20 s, 10% ΔF/F) in response to natural image sequences. **b**, Linear receptive fields (RFs) of the neurons in

**a** obtained by regularized reverse correlation (Methods). Scale bars, 20°. **c**, RFs of neurons from two mice at different ages. a.u., arbitrary units; red indicates ON subfield; blue indicates OFF subfield. **d**, **e**, Fraction of neurons with significant RFs (**d**, $\chi^2$ test) and RF size (**e**, rank-sum test) at eye opening and in more mature V1. Error bars, s.d.; P14–15, $n = 4$ mice; P28–35, $n = 5$ mice.

natural movies (signal correlation; Fig. 2c, d, f, h) and to the differences in their preferred orientation (Fig. 2g, i). We used natural movie signal correlation for comparison of response similarity not only because it was a good predictor of the similarity of the neurons' linear RFs (Supplementary Fig. 3), but because it also probably captures the similarity of feature selectivity in neurons with nonlinear RFs, which could not be estimated by reverse correlation.

The overall rate of connectivity was not significantly different between the two age groups (P13–15, 16.4%, 58 of 353 connections tested; P22–26, 21.7%, 64 of 295 connections tested; $P = 0.09$, $\chi^2$ test; Fig. 2e). Among the neurons recorded *in vitro*, 73% (104 of 143) and 56% (79 of 140) exhibited significant responses to the natural movie *in vivo* (Methods). As we reported previously[5], among responsive L2/3 pyramidal cells the connection probability increased steeply with increasing signal correlation at P22–26 ($P = 4.6 \times 10^{-4}$, Cochran–Armitage test; Fig. 2f). This was not the case at P13–15 ($P = 0.092$), when a much weaker trend was observed. Specifically, there were twice as many connections between highly correlated neuronal pairs (signal correlation, ≥0.1) in older V1 than at eye opening (P13–15, 19.4%, 19 of 98 tested; P22–26, 41.5%, 22 of 53 tested; $P = 0.0035$, $\chi^2$ test; Fig. 2f). Therefore, the functional selectivity of synaptic connections increased in the period after eye opening, as more connections formed selectively between neurons responding to similar stimulus features.

We further examined the refinement of connection specificity by relating the connection rate between reliably responsive, orientation-tuned neurons (P13–15, 43.4%, 62 of 143 neurons; P22–26, 57.9%, 81 of 140; Fig. 2g and Methods) to the difference in their preferred orientation. A significant decreasing relationship between connection probability and the difference in preferred orientation was present in more mature V1 but not at eye opening (P13–15, $P = 0.27$; P22–26, $P = 0.034$; Cochran–Armitage test; Fig. 2g). Together, these results indicate that at eye-opening the organization of synaptic connections between nearby L2/3 pyramidal neurons exhibits only weak functional specificity. After the onset of visual experience, connectivity increases specifically between neurons coding for similar visual features.

Previous studies suggest that bidirectional recurrent connections are overexpressed in some cortical networks[2,4] and that they are most frequent between L2/3 pyramidal cell pairs with similar visual responses in mature V1[5]. We examined whether a similar organization of bidirectional motifs is already present at eye-opening. In contrast to mature mice, visually naive mice did not exhibit a larger proportion of bidirectionally connected pairs between neurons with highly correlated responses to the natural movie (P13–15, $P = 0.27$; P22–26, $P = 0.01$; Cochran–Armitage test; Fig. 2h). Similar trends were found between neurons preferring similar orientations (P13–15, $P = 0.13$; P22–26, $P = 0.11$; Cochran–Armitage test; Fig. 2i). Therefore, this statistical feature of pairwise connectivity also refines after eye opening, such that a greater proportion of neurons with similar visual responses become bidirectionally connected (Fig. 2h, i).

We next tested for developmental changes in recurrent connectivity between neurons not reliably responsive to visual stimuli, which were encountered in similar proportions in both age groups (fraction of neurons not significantly responsive to repeated presentations of the natural movie: P13–15, 39%, 4,133 of 10,509; P22–26, 44%, 4,691 of 10,662). At P22–26, non-responsive neurons connected to each other at much lower rates than responsive neurons ($P < 0.01$, Tukey's HSD multiple-comparison test among proportions; Fig. 3a). At P13–15, however, responsive and non-responsive neurons formed recurrent connections at similar rates ($P > 0.05$; Fig. 3a). These data suggest that connections between L2/3 neurons not driven effectively by visual stimuli are selectively eliminated after eye opening ($P < 0.01$; Fig. 3a). This nonspecific-connection scheme at eye opening is consistent with the statistics of population activity during visual stimulation, which showed a twofold-higher total pairwise firing rate correlation at P13–15 than at P22–26 (median correlation: P13–15, 0.044; P22–26, 0.021; $P < 10^{-307}$, rank-sum test; Fig. 3b). Higher activity correlations at eye opening may allow connections to be maintained between neurons not reliably driven by visual stimuli. These connections are then lost as activity in the V1 network becomes progressively less correlated.

To obtain a mechanistic insight into the refinement of local recurrent connectivity after eye opening, we constructed a network model of the neocortex based on activity-dependent synaptic plasticity[27]. The model consisted of a recurrently connected cortical network of 18 excitatory and 5 inhibitory integrate-and-fire neurons (Methods). Cortical neurons received feedforward input from 500 presynaptic neurons, a subset of which exhibited spatially correlated activity during each iteration of the simulation (Fig. 4a). The weights of both recurrent and feedforward synapses were updated by a voltage-based spike-timing-dependent plasticity (vSTDP) learning rule[27]. Initially, neurons were seeded with RFs (Methods) and the weights of the recurrent network were drawn randomly from a uniform distribution (Fig. 4b, upper panels). Excitatory neurons in the recurrent network with the same RFs developed strong, mostly bidirectional connections (93.2%; proportions taken across 50 simulations; Fig. 4b, c). There was a strong decrease in connectivity between neurons that were not responsive to feedforward input (from 20.5% near the beginning of the simulation to 0.6% at the end; Fig. 4d) but not between neurons that were both responsive to feedforward input (decrease from 26.0% to 20.7%), consistent with experimental observations (Fig. 3a). To compare the model's behaviour further with our experimental data, we froze the feedforward and recurrent weights at three time points and measured the signal correlation between all responsive neuronal pairs. Higher signal correlations between neurons indicated a higher rate of connectivity at later but not earlier stages of network development (Figs 4e and 2f). The model also predicted the increase in bidirectional connections between neurons with high signal correlations at later stages of development (Figs 4e and 2h). These simulations suggest that feedforward connection patterns determine the structure of recurrent connectivity by activity-dependent mechanisms of synaptic plasticity.
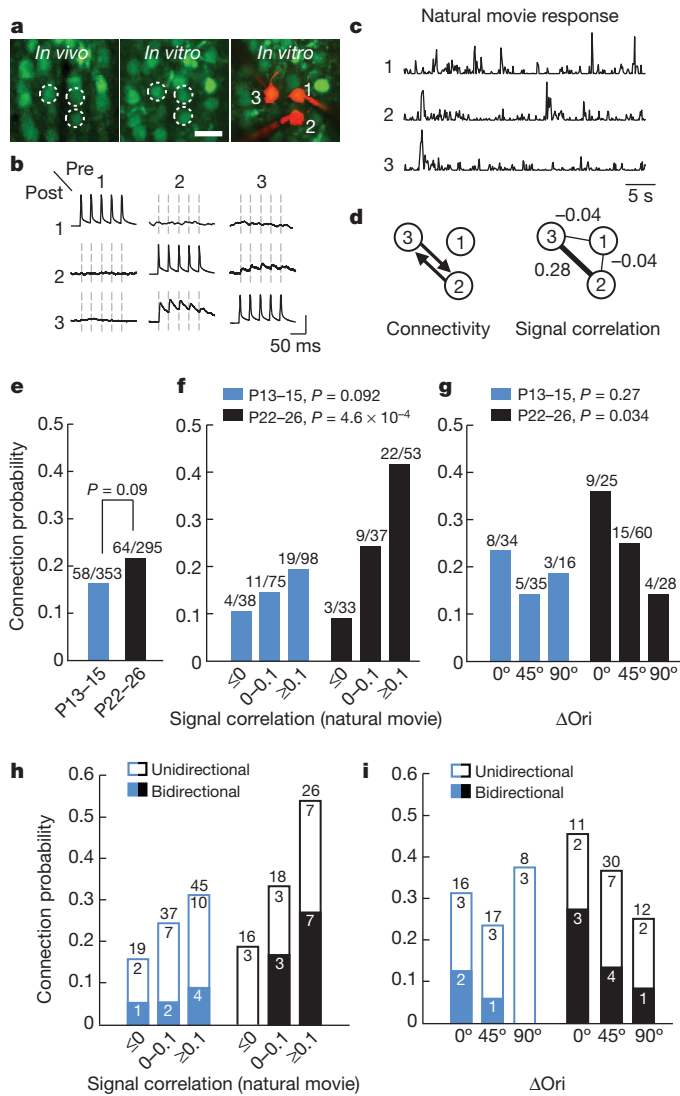
**Figure 2 | Functionally specific connectivity between L2/3 pyramidal cells is not apparent at eye opening.** **a**, Example triplet of neurons shown in a transformed *in vivo* image (left), in the brain slice (middle) and during whole-cell recordings (right). Scale bar, 30 μm. **b**, Membrane potential recordings from neurons shown in **a**. Evoked spikes and average traces of postsynaptic potentials. Dashed lines indicate timing of presynaptic spikes. Vertical scale bars, 80 mV for traces along the diagonal, 0.8 mV otherwise. **c**, Peristimulus time histogram of spikes inferred from calcium signals (arbitrary units) of the three neurons in response to a natural movie sequence (averages of six repetitions). **d**, Schematics of synaptic connectivity and *in vivo* signal correlations during natural movies for the three neurons in **a**. **e**, Overall connectivity rates at eye opening and in more mature V1; $\chi^2$ test. **f**, Relationship between connection probability and signal correlation of neuronal pairs significantly responsive to the natural movie across age; Cochran–Armitage test. **g**, Relationship between connection probability and difference in preferred orientation (ΔOri) among pairs in which both neurons were responsive and orientation selective (orientation selectivity index >0.4). **h**, **i**, The probability of observing uni- or bidirectionally connected pairs as a function of either signal correlation (**h**) or ΔOri (**i**). P13–15, n = 13 mice; P22–26, n = 18 mice.

Our results indicate that RFs exist before mature patterns of recurrent connectivity. However, transient electrical coupling via gap junctions between clonally related neurons contributes to shared feature selectivity and raises the possibility that intracortical connectivity may precede and instruct RF formation[7,9,28]. We extended our network model earlier in time to examine the mechanisms by which gap-junction coupling may influence the emergence of RFs and recurrent connectivity. In this model, early recurrent connectivity in the cortical
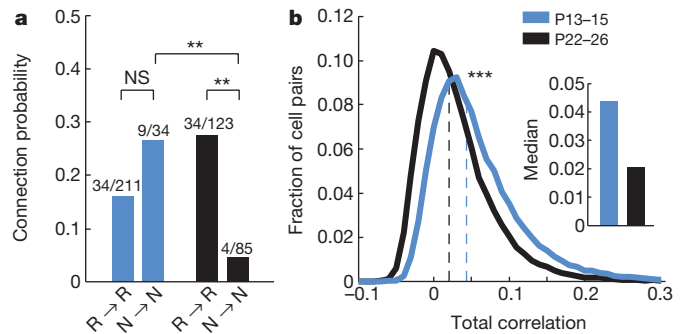


**Figure 3 | Developmental elimination of recurrent connections between non-responsive neurons.** **a**, Connection probability between neurons significantly responsive to the natural movie (R → R) and between non-responsive neurons (N → N) at two ages. **P < 0.01, Tukey's HSD multiple-comparison test among proportions; NS, not significant. **b**, Distribution of pairwise time-varying inferred firing rate correlation coefficients for all responsive cell pairs (to natural movies) separated by <50 μm. ***P < $10^{-307}$, rank-sum test.

network was provided by electrical gap junctions (Fig. 4f, g) and recurrent excitatory chemical synapses did not exist, approximating the organization of the mouse neocortex in the first postnatal week[7]. Early feedforward connections were randomly assigned (Fig. 4f, g) and their weights were updated according to the vSTDP rule. Cell pairs were more likely to stabilize the same set of feedforward inputs (that is, develop the same RF) if they had been connected by gap junctions (gap-junction coupled, 31.6%, 79 of 250 pairs; not gap-junction coupled, 4.1%, 305 of 7,400 pairs; $P < 0.001$, $\chi^2$ test; 50 simulations; Fig. 4h). We then removed the gap junctions, which disappear by the second postnatal week in mouse V1[7], and assigned random recurrent synaptic connections to neurons in the cortical network (Fig. 4f, g). Neurons sharing the same RF formed strong synaptic connections (Fig. 4c, g). Therefore, the functional specificity of recurrent connections was influenced indirectly by early gap-junction motifs (Fig. 4i), as electrically coupled neurons were first likely to develop the same RFs before becoming synaptically connected.

Separate simulations initiated with chemical connections revealed that early modifiable bidirectional chemical connections had no influence on either the formation of RFs or recurrent connectivity at the end of the simulation (probability of developing same RF: not connected, 5.5%, 270 of 4,918 pairs; bidirectional chemical connections, 3.8%, 11 of 288 pairs; $P = 0.22$, $\chi^2$ test; 50 simulations; Fig. 4h, i). Therefore, early initial biases in cortical connectivity may only influence functional circuit development if they exist as strong and stable connections when feedforward inputs are being selected. Although the absolute connectivity rates found experimentally were not perfectly replicated in the model (compare Fig. 2f with Fig. 4e), the connection probability between cells with similar visual responses was higher when assessed deeper in the acute slice, where connections are more likely to be preserved during cutting (supplementary fig. 6 of ref. 5).

We found that the functional specificity of local connections in mouse V1 was not apparent at eye opening despite the occurrence of highly selective responses to visual features. Although the overall rate of synaptic connectivity did not change after eye-opening, connections redistributed according to the following rules: more connections were added preferentially between neurons responding most similarly to visual stimuli, whereas connections were eliminated between cells not reliably responsive to visual stimulation. This result is surprising given existing theories of neural circuit formation, which suggest either that connections are initially exuberant and are subsequently 'pruned'[10,13] or that synapse number increases after the onset of sensory experience[11,14]. Instead, in local L2/3 networks we find a balanced restructuring of connectivity after eye opening. It remains
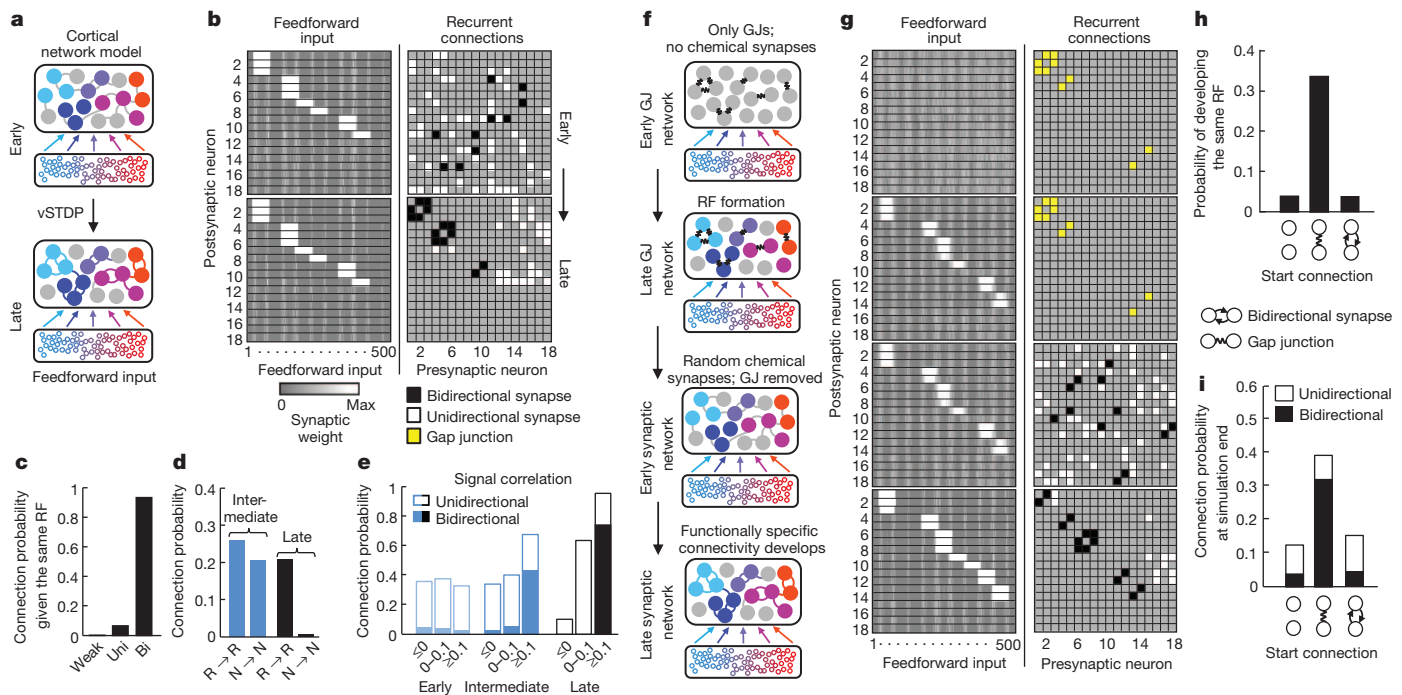
**Figure 4 | Feedforward input structure determines the functional organization of recurrent connectivity. a**, Sketch of the network model of functional microcircuit development based on vSTDP (see text for details). At the start of the simulation, cortical neurons were randomly connected but received spatially clustered input from a subset of presynaptic neurons. Both feedforward and recurrent connections were updated according to the vSTDP rule (Methods). **b**, Synaptic weight matrices of feedforward (left, reordered for display purposes) and recurrent (right) connections from an example network at the beginning and end of the simulation. Recurrent synaptic connections were classified as weak (light grey), unidirectional (white) or bidirectional (black). **c**, Probability of observing weak, unidirectional or bidirectional connections, at the end of the simulation, between neurons that start with the same RF. **d**, Connection probability of responsive (R→R) and non-responsive (N→N) neuronal pairs during and at the end of the simulation. **e**, Relationship

between connection probability and feedforward input-driven signal correlation at three time points in the simulation. **f**, Sketch of different stages of the network model extended to earlier developmental times. GJ, gap junction. **g**, Synaptic weight matrices from the example gap-junction network model. The recurrent network is initially connected with gap junctions (yellow) in the absence of chemical synapses. With time, neurons selected a spatially clustered set of feedforward inputs (RFs). Gap junctions were then removed and recurrent chemical connections were randomly assigned. The simulation was then continued as in **a** and **b**. **h**, Probability of developing RFs from the same set of feedforward inputs for pairs with no recurrent connections, gap junctions or early bidirectional connections (data from separate simulations) at the start of the simulation. **i**, Probability of developing shared connections depended on the starting connectivity. Data in **c–e**, **h** and **i** are from 50 network simulations.

to be seen whether similar mechanisms contribute to the elaboration of long-range connections in visual cortex of rodents and other mammals[22,29,30].

Functionally specific connection patterns between L2/3 pyramidal cells seem to be instructed by feedforward input (for example from layer 4 or the visual thalamus) only after RF formation. Our network model suggests that correlated firing driven by feedforward activity increases the functional specificity of recurrent connections by activity-dependent mechanisms of synaptic plasticity, which leads to the preferential formation of synapses between any neurons sharing similar RFs. The model can additionally explain how electrically coupled neurons early in development first develop similar feature selectivity and then preferential recurrent connectivity[7,9,28] (Fig. 4g–i).

Our data suggest that functionally organized connectivity between L2/3 pyramidal neurons is not necessary for establishing elemental RF properties at eye opening. Instead, it may contribute to the amplification of visually driven responses and thereby increase the robustness and reliability of cortical representation of sensory input with age (Supplementary Fig. 2c), which may be facilitated by the preferential formation of bidirectional connections between neurons with similar stimulus preferences (Fig. 2h, i). The role of inhibition for the maturation of visual responsiveness remains to be determined.

In conclusion, the patterning of recurrent cortical connectivity through the feedforward-driven, activity-dependent redistribution of connections may be a fundamental rule by which neurons link together into assemblies that process related information.

## METHODS SUMMARY

Responses to different visual stimuli in anaesthetized mouse V1 L2/3 cells were measured using *in vivo* two-photon calcium imagining as previously described[5,25]. Receptive fields were obtained by reverse correlation using a regularized pseudo-inverse method[24]. Synaptic connections were assayed by *in vitro* whole-cell recordings of a subset of neurons imaged *in vivo* and re-identified as previously described[5,25]. The incidence, strength and short-term dynamics of synaptic connections were related to visual response properties across age (Figs 2 and 3 and Supplementary Fig. 4). The network model consisted of 23 recurrently connected integrate-and-fire type neurons (18 excitatory, 5 inhibitory) receiving 500 feedforward inputs with neuronal dynamics and plasticity modelled as in ref. 27.

**Full Methods** and any associated references are available in the online version of the paper.

1. Binzegger, T., Douglas, R. J. & Martin, K. A. C. A quantitative map of the circuit of cat primary visual cortex. *J. Neurosci.* **24**, 8441–8453 (2004).
2. Song, S., Sjöström, P. J., Reigl, M., Nelson, S. & Chklovskii, D. B. Highly nonrandom features of synaptic connectivity in local cortical circuits. *PLoS Biol.* **3**, e68 (2005).
3. Brown, S. P. & Hestrin, S. Intracortical circuits of pyramidal neurons reflect their long-range axonal targets. *Nature* **457**, 1133–1136 (2009).
4. Perin, R., Berger, T. K. & Markram, H. A synaptic organizing principle for cortical neuronal groups. *Proc. Natl Acad. Sci. USA* **108**, 5419–5424 (2011).
5. Ko, H. *et al.* Functional specificity of local synaptic connections in neocortical networks. *Nature* **473**, 87–91 (2011).
6. Yoshimura, Y., Dantzker, J. L. M. & Callaway, E. M. Excitatory cortical neurons form fine-scale functional networks. *Nature* **433**, 868–873 (2005).
7. Yu, Y.-C. *et al.* Preferential electrical coupling regulates neocortical lineage-dependent microcircuit assembly. *Nature* **486**, 113–117 (2012).

8. Yuste, R., Peinado, A. & Katz, L. C. Neuronal domains in developing neocortex. *Science* **257,** 665–669 (1992).
9. Li, Y. *et al.* Clonally related visual cortical neurons show similar stimulus feature selectivity. *Nature* **486,** 118–121 (2012).
10. Katz, L. C. & Shatz, C. J. Synaptic activity and the construction of cortical circuits. *Science* **274,** 1133–1138 (1996).
11. White, L. E. & Fitzpatrick, D. Vision and cortical map development. *Neuron* **56,** 327–338 (2007).
12. Huberman, A. D., Feller, M. B. & Chapman, B. Mechanisms underlying development of visual maps and receptive fields. *Annu. Rev. Neurosci.* **31,** 479–509 (2008).
13. Innocenti, G. M. & Price, D. J. Exuberance in the development of cortical networks. *Nature Rev. Neurosci.* **6,** 955–965 (2005).
14. Purves, D., White, L. E. & Riddle, D. R. Is neural development Darwinian? *Trends Neurosci.* **19,** 460–464 (1996).
15. Mrsic-Flogel, T. D. *et al.* Homeostatic regulation of eye-specific responses in visual cortex during ocular dominance plasticity. *Neuron* **54,** 961–972 (2007).
16. Smith, S. L. & Häusser, M. Parallel processing of visual space by neighboring neurons in mouse visual cortex. *Nature Neurosci.* **13,** 1144–1149 (2010).
17. Bonin, V., Histed, M. H., Yurgenson, S. & Reid, R. C. Local diversity and fine-scale organization of receptive fields in mouse visual cortex. *J. Neurosci.* **31,** 18506–18521 (2011).
18. Hubel, D. H. & Wiesel, T. N. Receptive fields of cells in striate cortex of very young, visually inexperienced kittens. *J. Neurophysiol.* **26,** 994–1002 (1963).
19. Chapman, B. & Stryker, M. P. Development of orientation selectivity in ferret visual cortex and effects of deprivation. *J. Neurosci.* **13,** 5251–5262 (1993).
20. Krug, K., Akerman, C. J. & Thompson, I. D. Responses of neurons in neonatal cortex and thalamus to patterned visual stimulation through the naturally closed lids. *J. Neurophysiol.* **85,** 1436–1443 (2001).
21. Rochefort, N. L. *et al.* Development of direction selectivity in mouse cortical neurons. *Neuron* **71,** 425–432 (2011).
22. White, L. E., Coppola, D. M. & Fitzpatrick, D. The contribution of sensory experience to the maturation of orientation selectivity in ferret visual cortex. *Nature* **411,** 1049–1052 (2001).
23. Stosiek, C., Garaschuk, O., Holthoff, K. & Konnerth, A. *In vivo* two-photon calcium imaging of neuronal networks. *Proc. Natl Acad. Sci. USA* **100,** 7319–7324 (2003).
24. Smyth, D., Willmore, B., Baker, G. E., Thompson, I. D. & Tolhurst, D. J. The receptive-field organization of simple cells in primary visual cortex of ferrets under natural scene stimulation. *J. Neurosci.* **23,** 4746–4759 (2003).
25. Hofer, S. B. *et al.* Differential connectivity and response dynamics of excitatory and inhibitory neurons in visual cortex. *Nature Neurosci.* **14,** 1045–1052 (2011).
26. Reid, R. C. & Alonso, J. M. Specificity of monosynaptic connections from thalamus to visual cortex. *Nature* **378,** 281–284 (1995).
27. Clopath, C., Büsing, L., Vasilaki, E. & Gerstner, W. Connectivity reflects coding: a model of voltage-based STDP with homeostasis. *Nature Neurosci.* **13,** 344–352 (2010).
28. Ohtsuki, G. *et al.* Similarity of visual selectivity among clonally related neurons in visual cortex. *Neuron* **75,** 65–72 (2012).
29. Callaway, E. M. & Katz, L. C. Emergence and refinement of clustered horizontal connections in cat striate cortex. *J. Neurosci.* **10,** 1134–1153 (1990).
30. Ruthazer, E. S. & Stryker, M. P. The role of activity in the development of long-range horizontal connections in area 17 of the ferret. *J. Neurosci.* **16,** 7253–7269 (1996).

**Author Contributions** H.K. and S.B.H. performed the *in vivo* and *in vitro* experiments and data analysis. S.B.H. performed the RF mapping experiments, and L.C. analysed the RF data with help from J.A. L.C., C.B. and C.C. extended the network model originally developed by C.C. H.K., L.C., S.B.H. and T.D.M.-F. wrote the manuscript. All authors discussed the data and commented on the manuscript.

**Author Information** Reprints and permissions information is available at www.nature.com/reprints. The authors declare no competing financial interests. Readers are welcome to comment on the online version of the paper. Correspondence and requests for materials should be addressed to S.B.H. (s.hofer@ucl.ac.uk) or T.D.M.-F. (t.mrsic-flogel@ucl.ac.uk).

## METHODS

**Animals and surgical procedures.** All experimental procedures were carried out in accordance with institutional animal welfare guidelines and licensed by the UK Home Office. Experiments were performed on C57Bl/6 mice aged P13–15 and P22–35. Mice were initially anaesthetized with a mixture of fentanyl (0.05 mg kg$^{-1}$), midazolam (5.0 mg kg$^{-1}$), and medetomidine (0.5 mg kg$^{-1}$). At the time of imaging, the injectable anaesthetic had mostly worn off and light anaesthesia was maintained by isoflurane (0.3–0.5%) in a 3:2 mixture of O$_2$:N$_2$O delivered via a small nose cone. Surgery was performed as described previously[15]. Briefly, a small craniotomy (1–2 mm) was carried out over primary visual cortex and sealed after dye injection with 1.6% agarose in HEPES-buffered artificial cerebrospinal fluid (ACSF) and a cover slip.

*In vivo* **two-photon calcium imaging.** For bulk loading of cortical neurons, the calcium-sensitive dye Oregon Green BAPTA-1 AM (OGB-1 AM, Molecular Probes) was first dissolved in 4 µl DMSO containing 20% Pluronic F-127 (Molecular Probes), and further diluted (1/11) in dye buffer (150 mM NaCl, 2.5 mM KCl and 10 mM HEPES, pH 7.4) to yield a final concentration of 0.9 mM. Sulphorhodamine 101 (SR 101, 50 µM, Molecular Probes) was added to the solution to distinguish neurons and astrocytes[31]. The dye was slowly pressure-injected into the monocular region of right visual cortex at a depth of 170–200 µm with a micropipette (3–5 MΩ, 3–10 p.s.i., 2–4 min) under visual control by two-photon imaging (×10 water immersion objective, Olympus). Activity of cortical neurons was monitored by imaging fluorescence changes with a custom-built microscope and a mode-locked Ti:sapphire laser (Mai Tai, Spectra-Physics) at a wavelength of 830 or 930 nm through a ×40 water immersion objective (0.8 NA, Olympus). Scanning and image acquisition were controlled by custom software written in LABVIEW (National Instruments).

Visual stimuli were generated using the MATLAB (Mathworks) Psychophysics Toolbox[32,33], and were displayed on an LCD monitor (60-Hz refresh rate) positioned 20 cm from the left eye, roughly at 45° to the long axis of the animal, covering ~105° × 85° degrees of visual space. At the beginning of each experiment, the appropriate retinotopic position in visual cortex was determined using small grating stimuli at 12–24 neighbouring positions. The monitor was repositioned such that the preferred retinotopic position of most imaged neurons was roughly in the middle of the monitor.

Imaging frames of 256 × 256 pixels were acquired at 7.6 Hz while different visual stimuli, including naturalistic images and movies, and drifting gratings (see below) were presented. After each recording, the focal plane and imaging position was checked and realigned with the initial image if necessary. In combined *in vivo* functional imaging and *in vitro* connectivity assaying experiments, to obtain visually evoked responses from all neurons in a cortical volume of approximately 285 µm × 285 µm × 40–120 µm, images were recorded at 7 to 18 cortical depths with a spacing of 7 µm, starting at ~110 µm below cortical surface, a depth that corresponds to superficial L2/3 in mouse V1.

Image sequences were aligned for tangential drift and analysed with custom programs written in MATLAB and LABVIEW. Recordings with significant brain movements, vertical drift or both were excluded from further analysis. Cell outlines were detected using a semi-automated algorithm based on morphological measurements of cell intensity, size and shape, and were subsequently confirmed by visual inspection. After erosion of the cell-based regions of interest (to minimize influence of the neuropil signal around the cell bodies), all pixels within each region of interest were averaged to give a single time course ($\Delta F/F$), which was additionally high-pass-filtered at a cut-off frequency of 0.02 Hz to remove slow fluctuations in the signal. Spike trains were inferred from calcium signals using a fast non-negative deconvolution method which approximates the maximum a-posteriori spike train for each neuron, given the fluorescence observations[34]. This method yields spike probabilities (or inferred firing rate) linearly related to the number of action potentials per imaging frame[25].

**Receptive field measurement.** Receptive field data were acquired from four mice at eye opening (P14–15) and five mature mice (P28–35). Naturalistic image sequences (between 1,440 and 2,700 individual images) were presented on the monitor during two-photon calcium imaging. Images were shown at 2-s intervals (0.5-s presentation time, interleaved by a 1.5-s grey screen) for a total presentation time of between 0.83 and 1.5 h. After the onset of each natural image, 15 imaging frames were recorded at 7.6 Hz before the next image was presented. For each cell in the imaged region, the response to an image was calculated in the following way. Spike probabilities were inferred from calcium signals using the fast non-negative deconvolution method described above. For each visual stimulus, $k = 1, \ldots, N$, and each cell, $i = 1, \ldots, C$, the response to the stimulus can be expressed as $r(k, i, j)$ where $j = 1, \ldots, 15$ are the 15 imaging frames. An average population response was calculated: $R(j) = \sum_{k,i} r(k, i, j)/NC$. If the imaging frame, $J$, denotes the frame during which the peak average population response occurred (such that $R(J) = \max_j\{R(j)\}$), then the response of cell $i$ to stimulus $k$ was defined as $\sum_{j=J-1}^{J+1} r(k, i, j)/3$.

To estimate linear RFs, a regularized pseudo-inverse method[24] was used for reverse correlating neuronal responses with images of natural scenes. This algorithm regularizes the inverse problem by introducing a two-dimensional smoothness constraint on the linear RF; namely, the constraint is that the Laplacian of the RF should be close to zero at all points ($\nabla^2 RF = 0$). This method introduces a regularization parameter, $\lambda$, which balances the emphasis to be placed on fitting the data and the emphasis to be placed on the smoothness constraint.

Because this method introduces this free parameter, we performed the following analysis to choose the regularization parameter. For each cell and each regularization parameter, the naturalistic images and associated responses were separated into training (75% of the data) and test (remaining 25% of the data) data sets. Training data sets were chosen randomly and the remaining 25% of the data was placed into the test data set. Linear RFs were then calculated using the training data, and a sigmoid nonlinearity, described by the equation

$$P(x) = \frac{A}{1 + \exp(-\alpha x + \beta)}$$

(where $A$ is the amplitude, $\alpha$ determines the slope and $\beta$ determines the offset of the sigmoid), was then fitted to the training data to convert the linear predictions made by the RF into neuronal spike probabilities. Response predictions to the naturalistic images of the test data set were then made and the correlation coefficient between the actual and predicted responses was taken as a measure of RF prediction performance. This procedure was carried out for each cell and each regularization parameter 100 times. For each cell, the regularization parameter that maximized the RF prediction performance was chosen.

To assess whether the RF for a particular cell was significant, the response vector to the naturalistic image sequence was randomly shuffled and the reverse correlation was performed again, using the same regularization parameter, $\lambda$. This procedure was repeated 99 times to produce 100 shuffled RFs, RF$_{shuffled}$. From these shuffled RFs, the mean, $\mu_{shuffled}$, and standard deviation, $\sigma_{shuffled}$, across all pixels were calculated. An RF was defined to be significant if there were pixels that had absolute values greater than $\mu_{shuffled} + 6\sigma_{shuffled}$.

To fit the Gabor function, we used only the RFs determined to be significant by the previous analysis. The RF was parameterized in MATLAB by fitting a two-dimensional Gabor function using the Levenberg–Marquardt algorithm. The Gabor function is described by

$$G(x,y) = A \exp\left(-\frac{x'^2}{2\sigma_x^2} - \frac{y'^2}{2\sigma_y^2}\right) \cos(2\pi f x' + \varphi)$$

where

$$x' = (x - c_x)\cos(\theta) - (y - c_y)\sin(\theta)$$
$$y' = (x - c_x)\sin(\theta) + (y - c_y)\cos(\theta)$$

These equations describe an underlying two-dimensional cosine grating parameterized by $\theta$ (orientation), $f$ (spatial frequency) and $\varphi$ (phase), which is enveloped by a two-dimensional Gaussian function parameterized by $A$ (amplitude), $c_x$ and $c_y$ (centre of the Gaussian), and $\sigma_x$ and $\sigma_y$ (standard deviations of the Gaussian perpendicular to and parallel to the axis of the grating, respectively). Gabor fits were individually inspected to make sure they matched the RF (some Gabor fits were excluded at this point because they did not provide a good match to the RF: P14-15, 3 of 191 (1.6%); P28-35, 6 of 201 (3%)).

To quantify the shapes of RFs, the dimensionless measures $n_x = \sigma_x f$ and $n_y = \sigma_y f$ were used[35]. These values express the size of the Gaussian envelope in terms of the wavelength of the underlying cosine grating. For instance, $n_x = 1$ indicates that the standard deviation of the Gaussian perpendicular to the grating is equal to half a cycle of the underlying cosine grating. To get a measure of the size of the RF (Fig. 1 and Supplementary Fig. 1), the visual angle subtended by the Gabor fit along the axis perpendicular to the direction of the cosine grating was calculated. That is, if the eye of the mouse is at $(0, 0, 0)$ in space, the centre of the monitor is at $(0, 0, d)$ (where $d$ is the shortest distance to the mouse eye from the screen), the centre of the Gabor fit to the RF is at $(c_x, c_y, d)$, and the angle of orientation of the cosine grating on the screen is $\theta$, then the visual angle, $\alpha$, subtended by the Gabor was calculated as

$$\alpha = \arccos\left(\frac{u \bullet v}{||u|| \, ||v||}\right)$$

where $u = (c_x - \sigma_x \cos(\theta), c_y + \sigma_x \sin(\theta), d)$ and $v = (c_x + \sigma_x \cos(\theta), c_y - \sigma_x \sin(\theta), d)$. Receptive field similarity was calculated as the pixel–pixel correlation coefficient.

**Natural movie signal correlation.** Natural movies consisted of 40-s sequences of either moving scenes in a mouse cage or compilations of The Life of Mammals (BBC), adjusted to 70% mean contrast, continuously looped six times. Visual

responsiveness to natural movies was determined by the following procedure. For all stimulus repetitions, inferred spike trains were moving-average-filtered with a time window of three frames ($\sim$0.394 s). The smoothed firing rates at corresponding points of the stimulus were then treated as groups and tested for differences by one-way analysis of variance. Neurons with a $P$ value less than 0.01 (that is, those that exhibited consistently increased firing during at least one period of stimulus presentation) were considered significantly visually responsive. For pairs of significantly responsive neurons, the signal correlation was calculated as the Pearson's correlation coefficient of the averaged responses to the stimulus.

**Orientation tuning.** To measure the orientation preference and selectivity of neurons, square-wave gratings (0.035 cycles per degree, 2 cycles per second, 100% contrast) drifting in eight different directions were randomly interleaved, with the grating standing still for 1.4–1.9 s before moving for 0.9–1.5 s (six repetitions per grating). Responsive neurons that exhibited consistently increased firing during at least one time point of presentation of each grating were identified by one-way analysis of variance. Among cells responsive to grating stimuli ($P < 0.05$), the mean inferred firing rate during the presentation of a drifting grating was taken as the response to each stimulus. From each trial, we obtained one orientation tuning curve, and neurons were defined as reliably responsive if the mean cross-correlation between all pairs of curves obtained from different trials was greater than 0.1. Responses from different trials were then averaged to obtain the average orientation tuning curve for each neuron. This orientation tuning curve was then Fourier interpolated to 360 points, and the preferred direction was determined by the angle at which the interpolated tuning curve attained its maximum. The preferred orientation was taken as preferred direction modulo 180°. Orientation selectivity index (OSI) was calculated as $(R_{best} - R_{ortho})/(R_{best} + R_{ortho})$, where $R_{best}$ is the interpolated response to the preferred direction and $R_{ortho}$ is the average of interpolated responses to the directions orthogonal to the best-responding direction. When relating connection probability to orientation selectivity, neurons were defined as orientation selective if OSI $> 0.4$. To quantify neuronal response reliability, we calculated the coefficient of variation (s.d. divided by mean) from responses to the optimal grating direction.

***In vitro* whole-cell recording.** We carried out imaging experiments followed by whole-cell recordings *in vitro* at P13–15 and P22–26, using an approach described previously[5]. After two-photon calcium imaging of visual responses *in vivo*, small volumes of red fluorescent microspheres (Lumafluor) were injected into the imaged region to facilitate identification of the region in the slice tissue. The mouse brain was then rapidly removed to and dissected in ice-cold ACSF containing 125 mM NaCl, 2.5 mM KCl, 1 mM MgCl$_2$, 1.25 mM NaH$_2$PO$_4$, 2 mM CaCl$_2$, 26 mM NaHCO$_3$, 25 mM dextrose; 315–325 mOsm, bubbled with 95% O$_2$/5% CO$_2$, pH 7.4. Visual cortex slices (300 μm) were cut coronally (HM 650 V Vibration Microtome, MICROM) and were incubated at 34 °C for 30 min before they were transferred to the recording chamber. The slice containing the imaged region was identified by the presence of OGB-1 green fluorescence and the red microsphere injection site. To reveal the relative locations of cells, a detailed morphological stack of the slice was acquired with a custom-built microscope and a mode-locked Ti:sapphire laser (Chameleon, Coherent), at a wavelength of 830 nm, through a ×16 water immersion objective (0.8 NA, Nikon). Scanning and image acquisition were controlled by custom software written in LABVIEW.

Whole-cell recordings from two to six cells were carried out in regions identified by visually comparing image stacks obtained *in vivo* and *in vitro*, using red fluorescent microspheres and the pial surface as reference. Recordings were carried out in ACSF at 28 °C, using Multiclamp 700B amplifiers (Axon Instruments), and data was acquired using custom software running in IGOR PRO[36] (WaveMetrics Inc.) or MATLAB. Recording pipettes were filled with internal solution containing 5 mM KCl, 115 mM K-gluconate, 10 mM K-HEPES, 4 mM MgATP, 0.3 mM NaGTP, 10 mM Na-phosphocreatine, 0.1% w/v biocytin, 40 μM Alexa Fluor 594; 290–295 mOsm, pH 7.2. Junction potential was not corrected for. The chloride reversal potential was about −85.2 mV. Cells were approached under visual guidance using laser-scanning Dodt contrast. After breakthrough, the presence of synaptic connections was tested by evoking five spikes at 30 Hz in each cell, repeated 30 to 120 times, while searching for postsynaptic responses.

The paired-pulse ratio (PPR) was calculated as the amplitude of the second evoked excitatory postsynaptic potential (EPSP) divided by that of the first one. After connectivity mapping, step currents from 250 pA to 700 pA were injected in 50-pA increments if the input resistance was smaller than around 400 MΩ, and, if necessary (as indicated by early ceasing of firing due to inactivation of voltage-gated sodium channels), currents from −125 pA to 350 pA were injected in 25-pA increments for neurons with larger input resistance. Pyramidal neurons were identified from several parameters: their morphology in Alexa-594-filled image stacks (Fig. 2a); regular-spiking pattern on current injection; spike half-width ($>$1 ms); and, in the presence of connections, depolarizing postsynaptic potentials (Fig. 2b). To match the same neurons imaged *in vivo* and recorded from *in vitro*,

we performed three-dimensional image registration of *in vivo* and *in vitro* image stacks by affine transformation using custom-written MATLAB software subsequent to the experiment.

Connection probabilities were calculated as the number of connections detected over the number of potential connections assayed. Probabilities of unidirectional and bidirectional connections were calculated as the numbers of unidirectionally and, respectively, bidirectionally connected pairs divided by the total number of pairs. To relate connectivity to functional properties, the asymptotic Cochran–Armitage test for trend was used to test for the significance of linear trends[37]. Pairs in which a high-quality recording was achieved in only one cell (for example when the other cell was too depolarized or unhealthy, or the seal resistance was less than 1 GΩ) connectivity was assayed only in the direction from the unhealthy cell to the healthy cell, given that spikes could be evoked in both cells. Data from these pairs were included in the analysis of connection probability, but not in the analysis of the probability of finding bidirectional or unidirectional pairs. Only neuronal pairs in which both neurons were located at $>$60-μm depth from the slice surface and with an intersoma distance of $<$50 μm were included in the analysis.

The strength and short-term plasticity of synapses were also measured because these synaptic parameters affect the efficacy of presynaptic firing on postsynaptic partners. In P13–15 mice, connections between L2/3 pyramidal cells were significantly stronger (median EPSP amplitude: P13–15, 0.41 mV; P22–26, 0.20 mV; $P = 2.9 \times 10^{-4}$, rank-sum test; Supplementary Fig. 4a) and PPR was significantly lower (median PPR: P13–15, 0.87; P22–26, 1.13; $P = 6.2 \times 10^{-4}$, rank-sum test; Supplementary Fig. 4b) than in P22–26 mice, in line with previous reports[38]. However, in neither age group was there significant correlation between EPSP amplitude or PPR, on the one hand, and signal correlation or difference in preferred orientation, on the other (Supplementary Fig. 4c-f). Part of the connectivity data was published previously in ref. 5.

**Neuron model.** In the network model, the dynamics of the membrane potential, $u(t)$, of model neurons is described by the adaptive exponential integrate-and-fire model[39]:

$$C\frac{du}{dt} = -g_L(u - E_L) + g_L \Delta_T e^{(u - V_T)/\Delta_T} - w_{ad} + z + I$$

Here $C$ is the membrane capacitance, $g_L$ is the leak conductance, $E_L$ is the resting potential and $I$ is the stimulating current. The exponential term describes the activation of sodium current. The parameter $\Delta_T$ is called the slope factor and $V_T$ is the threshold potential. A hyperpolarizing adaptation current is described by the variable $w_{ad}$, which has dynamics

$$\tau_{w_{ad}} \frac{dw_{ad}}{dt} = a(u - E_L) - w_{ad}$$

where $\tau_{w_{ad}}$ is the time constant of the adaption of the neuron and $a$ is a parameter. Upon firing, the variable $u$ is reset to a fixed value, $V_{reset}$, whereas $w_{ad}$ is increased by an amount $b$. An additional current, $z$, which is set to a value $I_{sp}$ immediately after a spike occurs and otherwise decays with a time constant $\tau_z$, such that

$$\tau_z \frac{dz}{dt} = -z$$

was used to account for spike afterpotential[40]. Refractoriness is modelled with the adaptive threshold, $V_T$, which starts at $V_{T_{max}}$ after a spike and decays to $V_{T_{rest}}$ with a time constant $\tau_{V_T}$, such that

$$\tau_{V_T} \frac{dV_T}{dt} = -(V_T - V_{T_{rest}})$$

Parameters for the neuron model were taken from ref. 39, and $\tau_z$ was set to 40 ms in agreement with refs 36, 41 and was kept fixed throughout all simulations. We made the following choices: $C = 281$ pF, $g_L = 30$ nS, $E_L = -70.6$ mV, $\Delta_T = 2$ mV, $V_{T_{rest}} = -50.4$ mV, $\tau_{w_{ad}} = 144$ ms, $a = 4$ nS, $b = 0.0805$ pA, $I_{sp} = 400$ pA, $t_z = 40$ ms, $\tau_{V_T} = 50$ ms, $V_{T_{max}} = -30.4$ mV.

**Plasticity model.** Our plasticity model exhibits separate additive contributions to the plasticity rule, one for long-term depression (LTD) and another one for long-term potentiation[42] (LTP). Synaptic weights had hard bounds imposed at $w_{min}$ and $w_{max}$. For the LTD part, we assumed that presynaptic spike arrival at synapse $i$ induces the depression of the synaptic weight $w_i$ by an amount $-A_{LTD}[\bar{u}_-(t) - \theta_-]_+$. The brackets $[\ldots]_+$ indicate rectification, that is, any value $\bar{u}_- < \theta_-$ does not lead to a change[43]. The quantity $\bar{u}_-(t)$ is an exponential low-pass-filtered version of the postsynaptic membrane potential, $u(t)$, with time constant $\tau_-$, such that

$$\tau_- \frac{d\bar{u}_-(t)}{dt} = -\bar{u}_-(t) + u(t)$$

Because the presynaptic spike train is described as a series of short pulses at time $t_i^n$, $X_i(t) = \sum_n \delta(t - t_i^n)$, where $i$ is the index of the synapse and $n$ is the index that

counts the spike, the depression—that is, the change in $w_i$ due to LTD (indicated by the superscript minus sign)—is given by

$$\frac{dw_i^-}{dt} = -A_{LTD}(\bar{\bar{u}})X_i(t)[\bar{u}_- - \theta_-]_+$$

if $w_i > w_{min}$, where $A_{LTD}(\bar{\bar{u}})$ is an amplitude parameter that is under the control of homeostatic processes[44] and $\bar{\bar{u}}$ is the running average of depolarization of the postsynaptic neuron, averaged over a time scale of 1 s. The time scale of 1 s is not critical (100 s or more would be more realistic for homeostasis), but is convenient for the numerical implementation.

For the LTP part, we assumed that each presynaptic spike at the synapse $w_i$ increases the trace, $\bar{x}_i(t)$, of some biophysical quantity, which decays exponentially with a time constant $\tau_x$ (refs 45, 46), such that

$$\tau_x \frac{d\bar{x}_i(t)}{dt} = -\bar{x}_i(t) + X_i(t)$$

where $X_i(t)$ is the spike train defined above. Potentiation—the change in $w_i$ due to LTP (indicated by the superscript plus sign)—is given by

$$\frac{dw_i^+}{dt} = A_{LTP}\bar{x}_i(t)[u - \theta_+]_+[\bar{u}_+ - \theta_-]_+$$

if $w_i < w_{max}$. Here $A_{LTP}$ is a free amplitude parameter fitted to electrophysiology data[27] and $\bar{u}_+(t)$ is another low-pass-filtered version of $u(t)$, similar to $\bar{u}_-(t)$ but with a shorter time constant, $\tau_+$. Thus, positive weight changes can occur if the momentary voltage, $u(t)$, surpasses a threshold, $\theta_+$, and, at the same time, the average value, $\bar{u}_+(t)$, is greater than $\theta_-$.

The final rule used in the simulation was

$$\frac{dw_i}{dt} = -A_{LTD}(\bar{\bar{u}})X_i(t)[\bar{u}_- - \theta_-]_+$$
$$+ A_{LTP}\bar{x}_i(t)[u - \theta_+]_+[\bar{u}_+ - \theta_-]_+$$

combined with hard bounds $w_{min} \leq w_i \leq w_{max}$. For network simulations, $A_{LTD}(\bar{\bar{u}}) = A_{LTD}\bar{\bar{u}}^2/u_{ref}^2$, where $u_{ref}^2$ is a reference value. We made the following parameter choices for simulations: $\theta_- = -70.6$ mV, $\theta_+ = -45.3$ mV, $A_{LTD} = 14 \times 10^{-5}$ mV$^{-1}$, $A_{LTP} = 8 \times 10^{-5}$ mV$^{-2}$, $\tau_x = 15$ ms, $\tau_- = 10$ ms, $\tau_+ = 7$ ms.

**Network simulation.** In all simulations, 500 presynaptic Poisson neurons with firing rates $v_i^{pre}$ ($i = 1, ..., 500$) were connected to 18 postsynaptic excitatory neurons. The input rates $v_i^{pre}$ followed a Gaussian profile, that is, $v_i^{pre} = A \exp(-(i-\mu)^2/2\sigma^2)$, with variance $\sigma = 10$ and amplitude $A = 30$. The centre, $\mu$, of the Gaussian shifted randomly every 100 ms between ten equally distributed positions, each position occurring with equal probability. Circular boundary conditions were assumed, that is, neuron $i = 500$ was considered to neighbour neuron $i = 1$. Five inhibitory neurons were each driven by 14 excitatory neurons and projected onto 11 excitatory neurons. These connections were chosen randomly and were fixed with a weight equal to 1. Feedforward connections onto the inhibitory neurons were drawn from a uniform distribution on the interval $[0, 0.5]$ and were fixed for the duration of the simulation. The reference value was set to $u_{ref}^2 = 70$ mV$^2$. Parameters for the feedforward connections were chosen as for the plasticity model. The excitatory recurrent connections were plastic under the same rule and with the same parameters as the feedforward connections, but the amplitudes $A_{LTP}$ and $A_{LTD}$ were reduced by a factor of 100.

In the first set of simulations, feedforward weights were initialized with RF (weights taken from previous test simulations took values between 0 and 3, which were also the hard bounds). At the beginning of the simulation, recurrent excitatory connection weights were drawn randomly from a uniform distribution on the interval $[0, 0.75]$ (hard bounds were set to 0 and 0.75). At each time point during the simulation, noise current (Gaussian white noise) was independently injected into each cell in the recurrent network. In this and all subsequent networks, the model was run for 20 s of simulated time to allow the homeostatic dynamical variables to settle before the recurrent synaptic weights were reinitialized. The simulations were then run for another 1,000 s.

To calculate signal correlations in the network at three different time points (at the reinitialization of recurrent excitatory chemical synapses, 1 s of simulation

time later and at the end of the simulation), the weights were frozen and the same stimuli were played to assess the firing rate correlations across neurons. Two neurons were considered to be bidirectionally connected if both synaptic weights between them were >0.6, and were considered to be unidirectionally connected if only one of the synaptic weights was >0.6.

Responsiveness was determined in the following way: the feedforward weights onto each neuron were summed, to produce a single value for each cell. These values were then plotted on a histogram, which displayed a bimodal distribution. A threshold value was chosen between the two peaks of this bimodal distribution, to separate the cells into responsive and non-responsive. Feedforward weights were manually checked to make sure no cells with clear RFs were missed. Neuronal pairs whose RFs had a correlation coefficient of >0.85 were defined to have the same RF.

The recurrent gap-junction network began such that neurons 1 and 2, 3 and 4, and 5 to 7 were electrically coupled together in the stated combinations, and was run in this state for 200 s. There were no chemical synapses during this time. The gap-junction model was taken from ref. 47. The current from neuron $i$ to neuron $j$ was defined as $I_{ij}(t) = \alpha \sum_i \delta(t - t_i) - g_{gap}[u_j(t) - u_i(t)]$, where we chose $g_{gap} = 2$nS and chose $\alpha$ such that the spikelet was about 2 mV. The network was in this state for 200 s of simulation time (after the initial 20-s settling time), at which point gap junctions were removed and replaced with recurrent excitatory chemical connections with weights drawn randomly from a uniform distribution on the interval $[0, 0.75]$. After this time point, Gaussian white noise current stimulation was again provided to each cell in the recurrent network. The network was then run for another 800 s.

The comparison chemical network was run in the same manner as the gap-junction network except that a recurrent chemical network, with weights drawn randomly from a uniform distribution on the interval $[0, 0.75]$, replaced the recurrent gap-junction network during the first 200 s, and there was no replacement of the recurrent weights after this 200 s.

31. Nimmerjahn, A., Kirchhoff, F., Kerr, J. N. D. & Helmchen, F. Sulforhodamine 101 as a specific marker of astroglia in the neocortex in vivo. *Nature Methods* **1,** 31–37 (2004).
32. Brainard, D. H. The psychophysics toolbox. *Spat. Vis.* **10,** 433–436 (1997).
33. Pelli, D. G. The VideoToolbox software for visual psychophysics: transforming numbers into movies. *Spat. Vis.* **10,** 437–442 (1997).
34. Vogelstein, J. T. et al. Fast nonnegative deconvolution for spike train inference from population calcium imaging. *J. Neurophysiol.* **104,** 3691–3704 (2010).
35. Ringach, D. L. Mapping receptive fields in primary visual cortex. *J. Physiol. (Lond.)* **558,** 717–728 (2004).
36. Sjöström, P. J., Turrigiano, G. G. & Nelson, S. B. Rate, timing, and cooperativity jointly determine cortical synaptic plasticity. *Neuron* **32,** 1149–1164 (2001).
37. Agresti, A. *Categorical Data Analysis* 2nd edn 181–182 (Wiley-Interscience, 2002).
38. Frick, A., Feldmeyer, D. & Sakmann, B. Postnatal development of synaptic transmission in local networks of L5A pyramidal neurons in rat somatosensory cortex. *J. Physiol. (Lond.)* **585,** 103–116 (2007).
39. Brette, R. & Gerstner, W. Adaptive exponential integrate-and-fire model as an effective description of neuronal activity. *J. Neurophysiol.* **94,** 3637–3642 (2005).
40. Shouval, H. Z., Bear, M. F. & Cooper, L. N. A unified model of NMDA receptor-dependent bidirectional synaptic plasticity. *Proc. Natl Acad. Sci. USA* **99,** 10831–10836 (2002).
41. Badel, L. et al. Dynamic I-V curves are reliable predictors of naturalistic pyramidal-neuron voltage traces. *J. Neurophysiol.* **99,** 656–666 (2008).
42. O'Connor, D. H., Wittenberg, G. M. & Wang, S. S.-H. Dissection of bidirectional synaptic plasticity into saturable unidirectional processes. *J. Neurophysiol.* **94,** 1565–1573 (2005).
43. Artola, A., Bröcher, S. & Singer, W. Different voltage-dependent thresholds for inducing long-term depression and long-term potentiation in slices of rat visual cortex. *Nature* **347,** 69–72 (1990).
44. Turrigiano, G. G. & Nelson, S. B. Homeostatic plasticity in the developing nervous system. *Nature Rev. Neurosci.* **5,** 97–107 (2004).
45. Gerstner, W., Kempter, R., Van Hemmen, J. L. & Wagner, H. A neuronal learning rule for sub-millisecond temporal coding. *Nature* **383,** 76–78 (1996).
46. Pfister, J.-P. & Gerstner, W. Triplets of spikes in a model of spike timing-dependent plasticity. *J. Neurosci.* **26,** 9673–9682 (2006).
47. Ostojic, S., Brunel, N. & Hakim, V. Synchronization properties of networks of electrically coupled neurons in the presence of noise and heterogeneities. *J. Comput. Neurosci.* **26,** 369–392 (2009).